INTERNATIONAL JOURNAL FOR NUMERICAL METHODS IN FLUIDS
Int. J. Numer. Meth. Fluids 2006; **50**:1175–1191
Published online 7 September 2005 in Wiley InterScience (www.interscience.wiley.com). DOI: 10.1002/fld.1057

The energetics of wave-driven mean flow oscillations

Nils P. Wedi*,†

European Centre for Medium Range Weather Forecasts, Shinfield Park, Reading RG2 9AX, U.K.

SUMMARY

The celebrated laboratory experiment of Plumb and McEwan (*J. Atmos. Sci.* 1978; **35**:1827–1839) represents a dynamical analogue to the quasi-biennial oscillation (QBO), the dominant variability in the equatorial stratosphere. The experiment demonstrates the influence of small-scale fluctuations on the long-time behaviour of larger-scale flows. In the direct numerical simulation of the laboratory experiment Wedi and Smolarkiewicz (*Int. J. Numer. Methods Fluids* 2005; **47**:1369–1374) showed the occurrence of a number of internal gravity wave processes: wave reflection, wave–wave–mean flow interaction, critical-layer formation and subsequent wave breaking, all of which are found in the atmosphere. Here, a comprehensive investigation of the energetics of wave-driven mean flow oscillations is presented. The analysis confirms the accurate incorporation of the external forcing in the simulation, utilizing a generalized time-dependent coordinate transformation. An available potential energy analysis (*J. Fluid Mech.* 1995; **289**:115–128) is used to assess the process of fluid mixing and potential to kinetic energy exchange in wave–mean flow interactions. The results aid to clarify the physical mechanisms as well as the role of numerical dissipation for the onset and the development of zonal mean zonal flow oscillations and distinguish the accuracy of particular numerical choices for the simulation of wave–driven flow phenomena, i.e. flux-form Eulerian or semi-Lagrangian advection algorithms. Copyright © 2005 John Wiley & Sons, Ltd.

KEY WORDS: QBO; wave–wave and wave–mean flow interaction; wave breaking; turbulence; direct numerical simulation; MPDATA; flux-form finite volume; advective-form semi-Lagrangian; energy budget; reversible and irreversible energy flux

1. INTRODUCTION

One distinguishing aspect of atmospheric turbulence compared to stratified homogeneous shear flows is the existence of locally turbulent regions resulting from wave overturning and breaking, representing a far-field response to an internal or external forcing [1]. For example, one observes the interference of waves originating from different sources, wave reflection at internal or external boundaries, wave–mean flow interactions and wave dissipation due to critical

*Correspondence to: Nils P. Wedi, European Centre for Medium Range Weather Forecasts, Shinfield Park, Reading RG2 9AX, U.K.
†E-mail: wedi@ecmwf.int

Received 31 March 2005
Revised 15 June 2005
Accepted 25 June 2005

layer momentum flux changes. This transition from wave instabilities to turbulence for internal gravity waves has been comprehensively reviewed in [2]. A striking example of the influence of small-scale fluctuations on the larger-scale flow is the quasi-biennial oscillation (QBO), the dominant variability in the equatorial lower stratosphere [3]. The principal mechanism of these periodically reversing winds in the tropics was demonstrated in the laboratory experiment of Plumb and McEwan [4]. The laboratory analogue of the stratospheric equatorial oscillation consists of a cylindrical annulus filled with density-stratified salty water, forced at the lower boundary by an oscillating membrane. At sufficiently large forcing amplitude the wave motion generates a longer period zonal mean flow oscillation. The direct numerical simulation of the laboratory analogue exhibits a number of internal gravity wave processes, wave reflection, wave interference, wave–mean flow interaction, critical layer formation and subsequent wave breaking within this layer [5, 6]. Thus the laboratory experiment represents a canonical case of irreversible processes leading to the self-organization of new spatio-temporal structures [7]. In the experiment, a 'self-destructing' critical layer is formed dynamically by wave–wave interactions (i.e. $t = 235$ and 265 min in Figure 2), determining the subsequent temporal and spatial structure of the overall mean flow pattern: a mean shear layer forms, whereby the enhanced convergence of the wave-induced stress within the critical layer through wave breaking within and below propels a downward growth of the layer. The mean flow arriving at the oscillating membrane filters the waves of opposite direction to allow only waves with reversed phase speed. These waves subsequently initiate the same process in opposite direction resulting in the overall flow pattern depicted in plate (a) of Figure 1 (i.e. periodically reversing zonal mean zonal winds, see References [6, 8] for details). This particular experimental setup simplifies the analysis of the flow compared to the atmospheric QBO, since at any chosen time in the flow evolution only an externally forced single horizontal wave-number and a discrete range of vertical wave numbers are observed.

Laboratory experiments that isolate particular flow structures have long been regarded as complimentary tools for studying the behaviour of large scale geophysical fluids, such as the Earth's atmosphere. Here, we extend the use by means of direct numerical simulation, to enhance our physical understanding of the observed phenomena and to stress the role of the numerics in the simulated (canonical) flow evolution.

In this study, the particular focus is on the energetic evolution, as we seek to identify and quantify the individual processes and mechanisms (numerical or physical) through which they derive their energy. However, the use of volume averaged and accumulated quantities for the flow analysis at intermittent analysis times (typically available in long climate simulations) is problematic. The energetic analysis of the evolution equation of potential energy does not allow to readily distinguish reversible and irreversible processes [9]. Also energetically, relatively small instantaneous variations in the volume averaged integrals can have a substantial influence on the long-term flow evolution. Further, a temporal or spatial separation of the involved processes is often difficult in practice. There have been a number of investigations into the energetics of the transition to turbulence which consider either waves or turbulence [10]. Often a separation of a mean and a fluctuation is used, while further splitting into a wavy and a turbulent part by suitably averaging over a wavelength or cycle of the perturbation [11–13]. Using an averaging adjusted to the isolated problem at hand (e.g. wave breaking events at a pre-existing asymptotic critical level [11]) may provide more insight into the mechanisms of energy exchange. However, the universality of the method has been criticized for its applicability in practice, in particular in view of the role of buoyancy, due to the developing

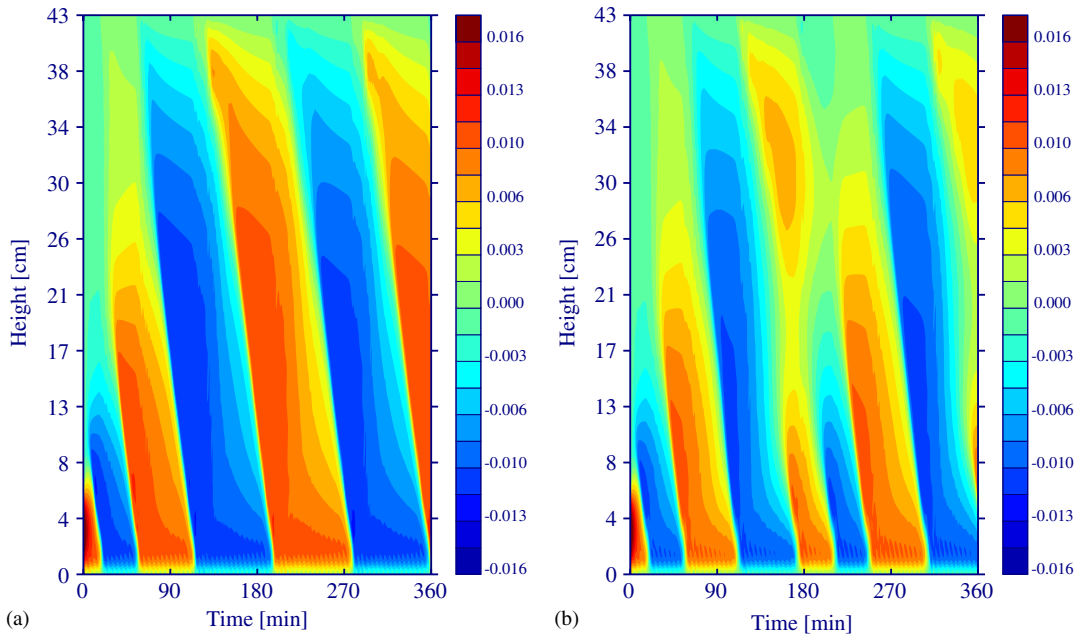

Figure 1. Time–height cross-section of the zonal mean flow velocity in the viscous 2D numerical simulation with noslip rigid boundaries, with a flux-form Eulerian advection scheme (plate (a)) and the same with an advective-form semi-Lagrangian setup (plate (b)).

(not *a priori* known) anisotropy of wave-driven flows and the intrinsic coupling of waves and turbulence in inhomogeneous stratified media. We failed to find an averaging procedure that would suitably separate the oscillating reversible and irreversible contributions to the total potential energy in our numerical simulations of the Plumb and McEwan experiment.

Instead, we apply the energy budget analysis described in Reference [9]. The authors use the idea of Lorenz [14] to subtract at every analysis time a particular energy from the reservoir of total potential energy. This subtracted energy would exist if the mass was redistributed such as to yield a horizontal, stable stratification. The resulting energy is called *available potential energy* [14]. The 'Carnot process' of generation of available potential energy and subsequent dissipation by turbulent diffusion (entropy production) has become a main paradigm underlying a variety of nonlinear fluid systems including the Earth and other planets [15]. The underlying energetic cycle is summarized in Figure 3. The diagram illustrates the different forms of energy in a Boussinesq system and their corresponding reversible and irreversible exchanges and external fluxes. In the context of the laboratory setup, the external energy symbolizes the storage reservoir of externally induced input to the flow via the oscillating membrane. The boundary oscillation enforces gravity waves in the stratified fluid, contributing to the available potential energy and the reversible exchange with kinetic energy through the buoyancy flux. As a result of the emerging non-linear flow disturbances the fluid is mixed contributing to the increase of background potential energy. Internal energy denotes the storage of energy within the fluid, with irreversible fluxes due to viscous dissipation of kinetic energy and irreversible

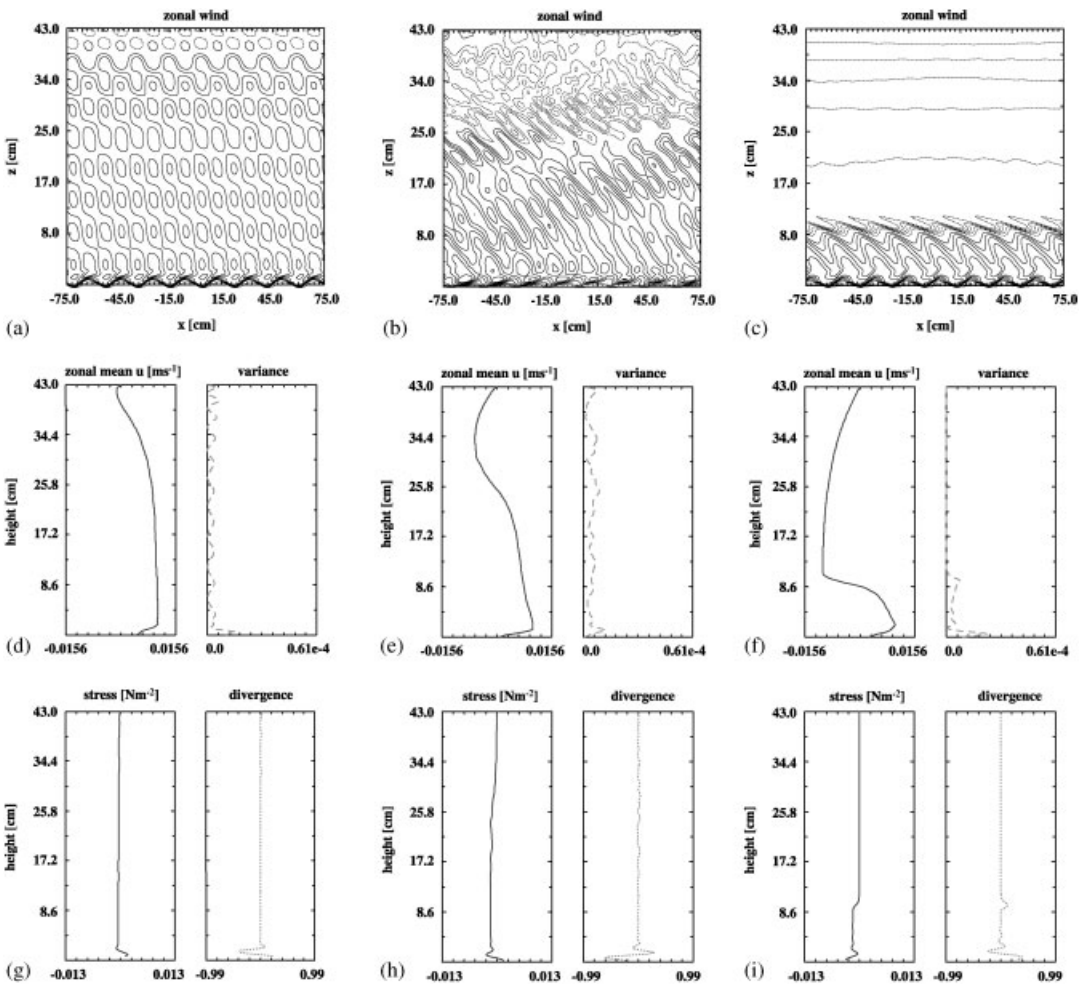

Figure 2. Zonal wind (a)–(c), the vertical profile of zonal mean wind (d)–(f) and its variance with height, and the Reynolds stress (g)–(i) and its vertical divergence, respectively, for the times (1–3) indicated in Figure 7. The contour interval in plate (a)–(c) is $2\,\mathrm{mm\,s^{-1}}$.

conversion from internal to potential energy, such as due to the diffusivity of salt in water. Section 3 defines the different forms of potential and kinetic energy in more detail.

The long-time behaviour of the repeating mean flow reversals in the direct numerical simulations of the laboratory experiment (cf. Figure 1) allows to identify repeating patterns in the above-described energetic cycle. They in return give insight into the mixing efficiency and the subsequent transitions from wavy structures to turbulence to changes in the overall background flow. Furthermore, our analysis allows to identify the role of the numerical formulation for the flow evolution, when comparing the application of a conservative flux-form finite volume method (Eulerian) with the corresponding trajectory based advective form (semi-Lagrangian).

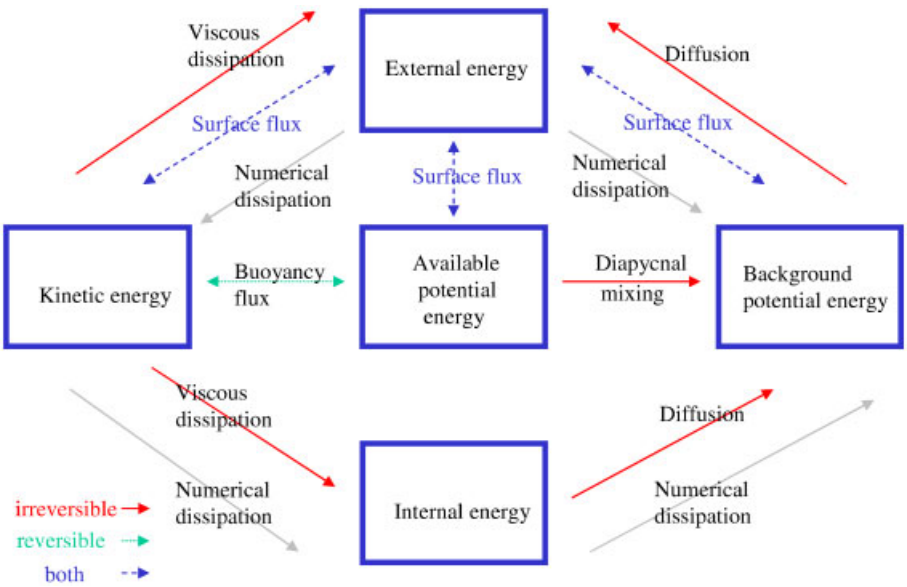

Figure 3. Energy diagram for density stratified Boussinesq flow adapted from Reference [9]. The energy within a fixed volume is stored as kinetic, available potential, background potential, or internal energy. Energy is input to the flow through surface fluxes. Reversible and irreversible energy exchanges occur through buoyancy flux, diabatic mixing, viscous dissipation, or diffusion.

The latter may have implications on the design of next-generation high resolution models of weather and climate.

The paper is organized as follows. Section 2 briefly summarizes the numerical setup of the simulations. Section 3 defines the computed energetic quantities. Section 4 discusses the time evolution of such volume averaged quantities in the context of the overall flow evolution from a physical and from a numerical perspective and Section 5 concludes the paper.

2. THE NUMERICAL MODEL

In the direct numerical simulation of the laboratory experiment of Plumb and McEwan [4] we simulate a non-rotating, density stratified viscous Boussinesq fluid, where the stratification is provided by a horizontally homogeneous, linear background density profile $\rho_e := \rho_0(1 - \mathscr{S}z)$ with $\rho_0 = 1025\,\mathrm{kg\,m^{-3}}$ and stratification $\mathscr{S} = 0.25\,\mathrm{m^{-1}}$, due to the varying salt concentration in water. The equations of motion are in this case given as

$$\nabla \cdot (\rho_0 \mathbf{v}) = 0 \tag{1a}$$

$$\frac{\mathrm{D}\mathbf{v}}{\mathrm{D}t} = -\nabla \frac{p'}{\rho_0} + \mathbf{g}\frac{\rho'}{\rho_0} + \frac{1}{\rho_0}\nabla \cdot \boldsymbol{\tau} \tag{1b}$$

$$\frac{\mathrm{D}\rho'}{\mathrm{D}t} = \kappa \nabla^2 \rho' - \mathbf{v} \cdot \nabla \rho_e \tag{1c}$$

Here, the operators $\mathrm{D}/\mathrm{D}t$, ∇, and $\nabla\cdot$ symbolize the material derivative, gradient, and divergence; $\mathbf{v}$ denotes the velocity vector; ρ' and p' denote, respectively, density and pressure perturbations with respect to the static ambient state described by ρ_e; $\mathbf{g}$ symbolizes the gravity vector, and ρ_0 a constant reference density. $\nabla\cdot\boldsymbol{\tau}$ is the divergence of the viscous stress tensor (a kinematic viscosity $\nu = 1.004\times10^{-6}\,\mathrm{m^2\,s^{-1}}$ is assumed); and κ $(=1.5\times10^{-9}\,\mathrm{m^2\,s^{-1}})$ is the diffusivity of salt in water.

Equations (1) are formulated in time-dependent curvilinear coordinates $(\bar{x},\bar{z},\bar{t})$ [16, 17], employing the generalized Gal–Chen coordinate transformation

$$\bar{t}=t,\quad \bar{x}=x,\quad \bar{z}=H_0\frac{z-z_s(x,t)}{H_0-z_s(x,t)} \tag{2}$$

whose theoretical development and efficient numerical implementation were discussed thoroughly in Reference [18]. The transformation (2) implies the addition of a regularly oscillating external forcing of the form

$$z_s(x,t)=\varepsilon\,\sin(kx)\sin(\omega_0 t) \tag{3}$$

with amplitude $\varepsilon=0.008\,\mathrm{m}$, wavenumber $k=2\pi 8/L_x$, and forcing frequency $\omega_0=0.43\,\mathrm{s^{-1}}$; $L_x=1.517388\,\mathrm{m}$ denotes the zonal domain length (see Reference [5] for a description of a 3D forcing). For simplicity, we consider here only the equatorial x–z plane, representative of the mid-channel of the cylindrical annulus in the laboratory. A horizontally periodic domain is used with 383×188 grid intervals, domain height $H_0=0.43\,\mathrm{m}$, and rigid noslip boundaries. The zonal mean zonal flow oscillation was started with an initial flow in the near-membrane layers $(d_0=0.06\,\mathrm{m})$ using $u_e=u_0[1-0.5\delta(1+\tanh(z-d_0)/\gamma)]$ with $u_0=0.02\,\mathrm{m\,s^{-1}}$, $\delta=0.9999999$, and $\gamma=\Delta z$. A time step of 0.05 s was used and simulations were run for upto 6 h. While not quantitatively comparable to 3D simulations, it is shown in Reference [6] that 2D numerical simulations of the Plumb and McEwan laboratory experiment exhibit a similar time evolution based on essentially the same physical processes.

The prognostic equations in (1) may be written in a compact conservation-law form using the transformed coordinates in (2) as

$$\frac{\partial\rho^*\psi}{\partial\bar{t}}+\bar{\nabla}\cdot(\rho^*\,\bar{\mathbf{v}}^*\psi)=\rho^*R \tag{4}$$

where $\bar{\nabla}:=(\partial/\partial\bar{x},\ \partial/\partial\bar{z})$, $\rho^*=\rho_0\bar{G}$, and ψ symbolizes a physical velocity component or density perturbation; here $\bar{G}$ denotes the Jacobian of the transformation. R summarizes the rhs of the equations in (1) (see Reference [16] for details). In (4), the advecting contravariant velocity $\bar{\mathbf{v}}^*$ is related to the physical velocity components v^k as

$$\bar{v^*}^k:=\mathrm{d}\bar{x}^k/\mathrm{d}\bar{t}=\frac{\partial\bar{x}^k}{\partial t}+\tilde{G}^j_n v^n \tag{5}$$

where $\tilde{G}_j{}^k:=(\partial\bar{x}^k/\partial x^j)$ are renormalized elements of the Jacobian, and $j,k=1,3$ correspond to the $\bar{x},\bar{z}$ components, respectively (summation is implied by the repeated index n).

Alternatively, the same prognostic equations can be formulated in Lagrangian form

$$\frac{\mathrm{d}\psi}{\mathrm{d}\bar{t}} = R \tag{6}$$

The nonoscillatory forward-in-time (NFT)[‡] approximation (cf. Reference [19] for a recent review) of either formulation—flux-form Eulerian [20] for (4), or semi-Lagrangian [21] for (6)—can be written compactly as

$$\psi_i^{n+1} = \mathrm{LE}_i(\tilde{\psi}) + 0.5\Delta t R_i^{n+1} \tag{7}$$

Here, we denote ψ_i^{n+1} as the solution at the grid point $(\bar{t}^{n+1}, \bar{\mathbf{x}}_i)$; $\tilde{\psi} := \psi^n + 0.5\Delta t R^n$; and LE denotes a NFT transport operator. In the Eulerian scheme, LE integrates the homogeneous transport equation (4), i.e. LE advects $\tilde{\psi}$ using a fully second-order-accurate multidimensional MPDATA advection scheme [19, 22]. In the semi-Lagrangian algorithm, LE remaps transported fields, which arrive at the grid points $(\bar{t}, \bar{\mathbf{x}}_i)$, to the departure points of the flow trajectories $(\bar{t}^n, \bar{\mathbf{x}}_0(\bar{t}^{n+1}, \bar{\mathbf{x}}_i))$ also using MPDATA type advection schemes [21, 23]. MPDATA is a finite-difference algorithm for approximating the advective terms in fluid equations. The solution procedure of MPDATA is iterative with a first pass using a simple donor cell approximation which is positive definite but only first-order accurate. In one dimension equation (4) (assuming $R = 0$, $\rho^* = 1$ for simplicity) takes the form

$$\psi_i^{n+1} = \psi_i^n - [F(\psi_i^n, \psi_{i+1}^n, \mathscr{C}_{i+1/2}) - F(\psi_{i-1}^n, \psi_i^n, \mathscr{C}_{i-1/2})] \tag{8}$$

where the flux function F is defined in terms of the local Courant number $\mathscr{C} \equiv u\Delta t/\Delta x$ by

$$F(\psi_L, \psi_R, \mathscr{C}) \equiv [\mathscr{C}]^+ \psi_L + [\mathscr{C}]^- \psi_R \tag{9}$$

with $[\mathscr{C}]^+ \equiv 0.5(\mathscr{C} + |\mathscr{C}|)$ and $[\mathscr{C}]^- \equiv 0.5(\mathscr{C} - |\mathscr{C}|)$. The second pass increases the accuracy by estimating and compensating the truncation error of the first pass to higher order. The scheme is reapplied using antidiffusive advective velocities, which are derived analytically from the advected field, and based on the truncation error analysis of the donor cell scheme [22]. All forcings on the rhs of Equation (7) are treated implicitly. Together with the curvilinearity of the coordinates, this leads to a complicated elliptic problem for pressure (see Appendix A in Reference [16] for the complete description) solved iteratively using the preconditioned generalized conjugate-residual approach—a nonsymmetric Krylov-subspace solver [24]. The viscous and diffusive terms are computed to first-order accuracy, assuming $\nabla \cdot \boldsymbol{\tau}^{n+1} = \nabla \cdot \boldsymbol{\tau}^n + \mathscr{O}(\Delta t)$ (and similar for $\kappa\nabla^2\rho'$); see Section 3.5.4 in Reference [22]. The 2D simulations shown have been performed on 16 processors of an IBM power4 cluster, using typically 2 h elapsed time per simulated hour.

[‡] 'Nonoscillatory' refers to monotone schemes, e.g. total variation diminishing (TVD), flux-corrected transport (FCT), and various flux-limited and sign-preserving schemes, that suppress/reduce/control numerical oscillations characteristic of higher order linear schemes. 'Forward-in-time' labels a class of generalized Lax–Wendroff type methods.

3. ENERGY ANALYSIS

The perturbation potential energy may be defined as the volume integral

$$E_p = g \int_V \rho' z \, \mathrm{d}V \tag{10}$$

Note that ρ_e has been subtracted in the volume averaged quantities E_p in Equation (10), E_b in Equation (14), and the buoyancy integral in Equations (12) and (13), to enhance the direct comparability with other equation terms. The kinetic energy is given as

$$E_k = \frac{\rho_0}{2} \int_V (u^2 + v^2 + w^2) \, \mathrm{d}V \tag{11}$$

An equation for the time rate of change of kinetic energy can be derived by taking the scalar product of the momentum equation (1b) with the wind vector $\mathbf{v}$ and the definition (11) (see References [9, 25] and references therein):

$$\frac{\mathrm{d}}{\mathrm{d}t} E_k = - \oint_S \left[p' \mathbf{v} + \frac{\rho_0}{2} \mathbf{v}(u^2 + v^2 + w^2) - \mathbf{v} \cdot \boldsymbol{\tau} \right] \cdot \hat{\mathbf{n}} \, \mathrm{d}S - \int_V g \rho' w \, \mathrm{d}V - \mathscr{D} \tag{12}$$

Here the first term on the right-hand side gives the reversible rate of change of kinetic energy from pressure work and advection, and the irreversible viscous diffusion of energy across the bounding surface S. The second term denotes the reversible exchange with potential energy via buoyancy and the last term $\mathscr{D}$ symbolizes the irreversible exchange of kinetic to internal energy through viscous dissipation. Consistent with its numerical evaluation in the model we computed only the total effect of viscosity as a volume integral of the viscous term $\int_V \mathbf{v} \cdot \nabla \cdot \boldsymbol{\tau}$. Similarly, an evolution equation for potential energy (10) is derived from the continuity equation (1a) and gz times the thermodynamic equation (1c)

$$\begin{aligned} \frac{\mathrm{d}}{\mathrm{d}t} E_p = &- \oint_S gz\rho \mathbf{v} \cdot \hat{\mathbf{n}} \, \mathrm{d}S + \int_V g \rho' w \, \mathrm{d}V + \kappa g \oint_S z \nabla \rho \cdot \hat{\mathbf{n}} \, \mathrm{d}S \\ &- \kappa g A_{xy} (\langle \rho_{\mathrm{top}} \rangle_{xy} - \langle \rho_{\mathrm{bottom}} \rangle_{xy}) \end{aligned} \tag{13}$$

Here, the first two terms on the right-hand side denote the reversible change of potential energy via the advective flux through the bounding surface S and via buoyancy. The last two terms specify the irreversible rate change due to diffusive mass fluxes across the surface S and the conversion rate from internal to potential energy; in the x–z plane the surface area is simply $A_{xy} = L_x$, and the surface area average is $\langle \rho \rangle_{xy} := 1/A_{xy} \int_A \rho \, \mathrm{d}x \, \mathrm{d}y$. Again, consistent with the numerical evaluation in the model, we computed only the total effect of diffusion from the volume integral $\int_V gz \nabla^2 \rho$. The diffusive surface flux is then determined from the difference of the total effect of diffusion and the last term on the right-hand side in (13).

As pointed out by Winters *et al.* [9] the evolution equation (13) does not readily allow to identify all reversible and irreversible dynamic processes, in particular the translation of buoyancy. Instead, the authors make use of a reconstructed reference state of minimum gravitational potential energy to separate diabatic (i.e. fluid mixing) and adiabatic processes. An analytic justification of this separation is given in Reference [9]. Numerically, we approximate this reference state at every time step by sorting all discrete fluid elements and stably

restratifying (from left to right) with heaviest elements at the bottom and lighter elements above. Using the approximate density distribution ρ_* obtained in this way, the *background potential energy* can be computed as

$$E_b = \int_V gz(\rho_* - \rho_e)\,\mathrm{d}V \tag{14}$$

and the *available potential energy* E_a can be obtained using (10) and

$$E_p = E_b + E_a \tag{15}$$

Following the derivations in Reference [9] one may obtain an evolution equation for the background potential energy of the form

$$\frac{\mathrm{d}}{\mathrm{d}t} E_b = S_{\mathrm{adv}} + S_{\mathrm{diff}} - \kappa g \int_V \left(\frac{\mathrm{d}\rho_*}{\mathrm{d}z}\right)^{-1} |\nabla\rho|^2\,\mathrm{d}V \tag{16}$$

where S_{adv} and S_{diff} denote advective and diffusive fluxes across the bounding surface S and the last term on the right-hand side gives the irreversible rate of change of potential energy due to material changes of density within the volume V, called *diapycnal mixing* [9]. Here, the concept of irreversible mixing readily distinguishes the mechanism from reversible exchanges of potential energy such as the buoyancy flux.

4. DISCUSSION

Figure 4, plate (a) in Figures 5 and 6 summarize the time evolution of the individual contributions to the kinetic and potential energy budget for the flux-form Eulerian case. Trends of total, kinetic and potential energy are also shown for the six hour integration period. Comparing with the time–height evolution of the mean flow in Figure 1 one can approximately identify the points of flow reversal as the decline of increased values of available potential energy. A comparison of the 'transient' energies in Figure 7 together with the different flow phases in Figure 2 reveals that peaks of available potential energy coincide with a larger vertical extent of free wave propagation. Following Reference [12] we additionally divided the total kinetic energy into a time mean

$$\bar{K} = \tfrac{1}{2}\langle\, \bar{\mathbf{v}}^t\, \bar{\mathbf{v}}^t \rangle_{xz} \tag{17}$$

and a transient part

$$K' = \tfrac{1}{2}\langle \overline{\mathbf{v}'\mathbf{v}'}^t \rangle_{xz} \tag{18}$$

where $\bar{\mathbf{v}}^t$ denotes a time mean velocity over a suitable period (i.e. 4–8 analysed values) and $\mathbf{v}' := \mathbf{v} - \bar{\mathbf{v}}^t$ denotes the corresponding fluctuation; here $\langle\rangle_{xz} := \int\int()\,\mathrm{d}A$ denotes an average over the two-dimensional domain. It can be seen in Figure 7 that both the transient kinetic energy and the absolute of the vertically integrated Reynolds stress follow similar patterns as the available potential energy. This provides three inherently different volume-averaged means, characterizing the same flow evolution. Relative minima are associated with wave interference and depend also on the periodicity of the buoyancy flux (compare to Figure 6).

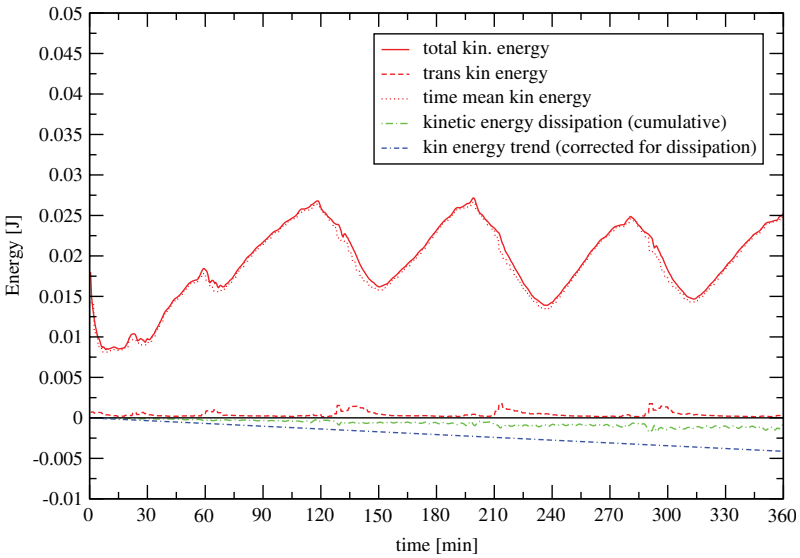

Figure 4. Total, time mean, and transient kinetic energy together with the irreversible, cumulative, viscous dissipation effect for the flux-form Eulerian case. The decaying trend of total kinetic energy is also shown.

The available potential energy becomes negative once a critical shear layer has formed. This happens in our simulation at approximately half the total vertical domain size (≈ 22 cm). Once the shear layer propagates downward this coincides with decreasing values of the vertically integrated Reynolds stress and decreasing values of transient kinetic energy. In comparison, the cumulative rates of the irreversible fluxes of diffusion and diapycnal mixing shown in plate (b) of Figure 5 exhibit a nearly constant growth. The rate of diapycnal mixing is upto 30 times larger compared to the rate of viscous total kinetic energy dissipation (cf. Figure 4), indicating a dominant role of diabatic fluid mixing for the background potential energy budget throughout the simulation. However, this does not necessitate a dominant role in the overall flow evolution.

The potential and kinetic energies and the instantaneous and cumulative effects of the reversible and irreversible rates have been used in order to assess the effect of numerical dissipation while accounting for all physical processes as depicted in Figure 3. A summary of the reversible fluxes depicted in the diagram are shown in Figure 6 for a selected time period. It can be seen that the magnitude of the surface flux, calculated via the advective right-hand side terms in (12) and (13), which feeds the available potential energy and the reversible exchange with kinetic energy, is nearly equivalent to the buoyancy flux (the second right-hand side term in (13)). The reversible buoyancy flux has a period of 8.5 min compared to the mean flow reversal period depicted in Figure 1 of 2.5 h, which indicates the two dominant time scales in the energetic evolution. Figure 4 gives an overview of the kinetic energy over a period of 3 h of simulation, i.e. 432 000 time steps. The trend of total energy (the sum of the potential and kinetic energy trends) is shown in plate (a) of Figure 5 as the thick line. Trends have been calculated for easier separation of the individual cumulative contributions from the

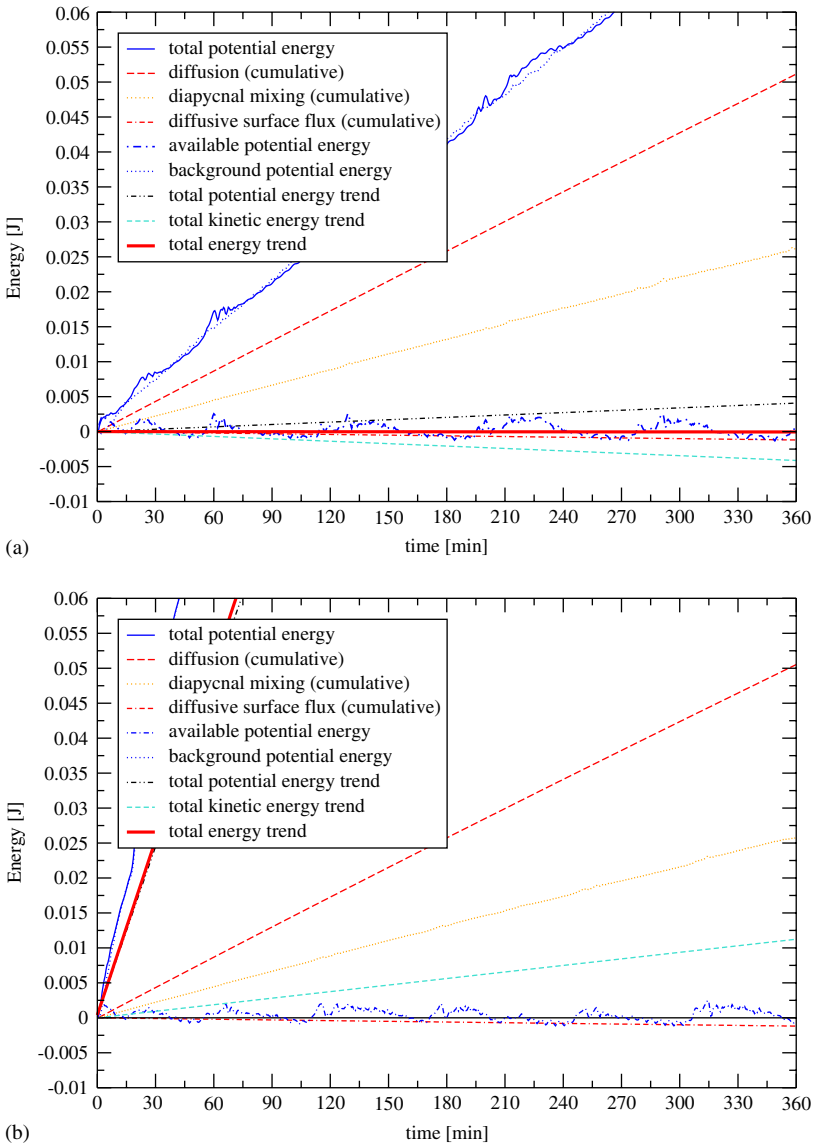

Figure 5. Plate (a) (top) shows the potential energy budget for the flux-form Eulerian case: total, available, and background potential energy, respectively. The irreversible cumulative effects of diffusion and trends of total, kinetic and potential energy are also shown. In comparison, plate (b) (bottom) represents the potential energy budget for the semi-Lagrangian advection case.

natural larger scale fluctuation of the flow given by the reversing zonal mean flow pattern. The potential energy trend has been calculated as a linear regression of the residual background potential energy after subtracting the cumulative effects of dissipation and diapycnal mixing. The kinetic energy trend has been calculated using a linear regression (discarding the first

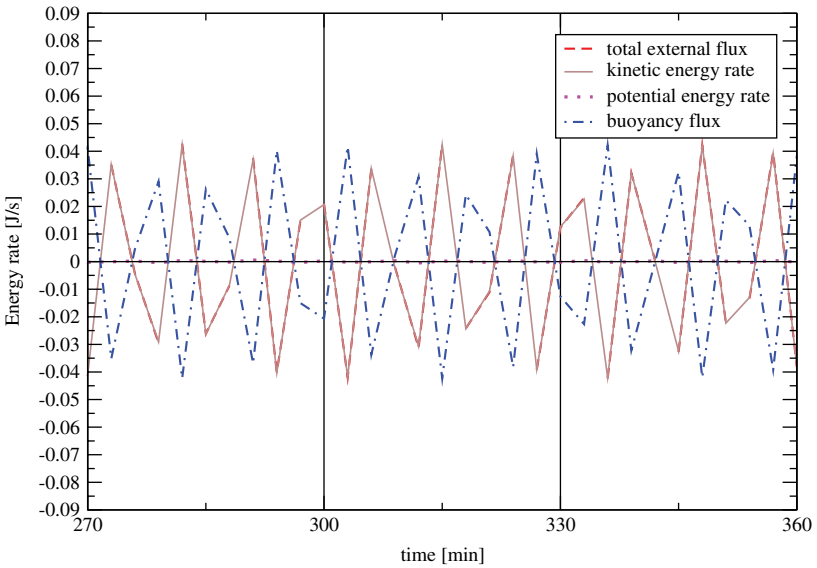

Figure 6. Exchange rates of energy for a selected period. The exchange rates are dominated by high frequency (≈3.5 buoyancy flux periods per 30 min) reversible oscillations. The instantaneous total kinetic energy rate is of the same size and opposite to the buoyancy flux. The instantaneous total potential energy rate is near zero due to the balance of the buoyancy term and the advective surface flux of the same size. The irreversible exchange rates are too small to be seen and are visualised through their respective cumulative effect in Figures 4 and 5.

160 points) of a 130 point running mean of kinetic energy, where the initial value has been subtracted. After subtraction of all physical contributions to the rates of potential and kinetic energy we find a residual (numerical) loss of kinetic energy of $\approx -5. \times 10^{-5}\%$ of the initial kinetic energy per time step. This may be compared with a loss of kinetic energy in the numerical weather prediction model at ECMWF, which is $\approx -2.7 \times 10^{-4}\%$ of the initial kinetic energy per time step. The loss is compensated by an almost equal amount of residual (numerically generated) potential energy growth as can be seen in plate (a) of Figure 5. The total energy residual is $\approx 1. \times 10^{-10}$ J per time step which is in the order of round-off errors. The Eulerian formulation of the model therefore conserves the total energy invariant of the analytic Boussinesq equations to the order of round-off errors. This verifies the negligible amount of any artificial energy source or sink terms other than the external surface fluxes (via the oscillating membrane).

The same analysis has been performed for the corresponding simulation using the semi-Lagrangian advection scheme. As can be seen from plate (b) in Figure 5, the accumulated physical irreversible rates (i.e. diapycnal mixing and cumulative diffusion) are very similar. We find that the standard deviation of the instantaneous reversible buoyancy flux for the semi-Lagrangian case is larger than the Eulerian counterpart and grows in time, whereas in the Eulerian case the variations around the mean appear to settle to a constant and smaller value. There is an irreversible growth of the kinetic energy in the semi-Lagrangian case of

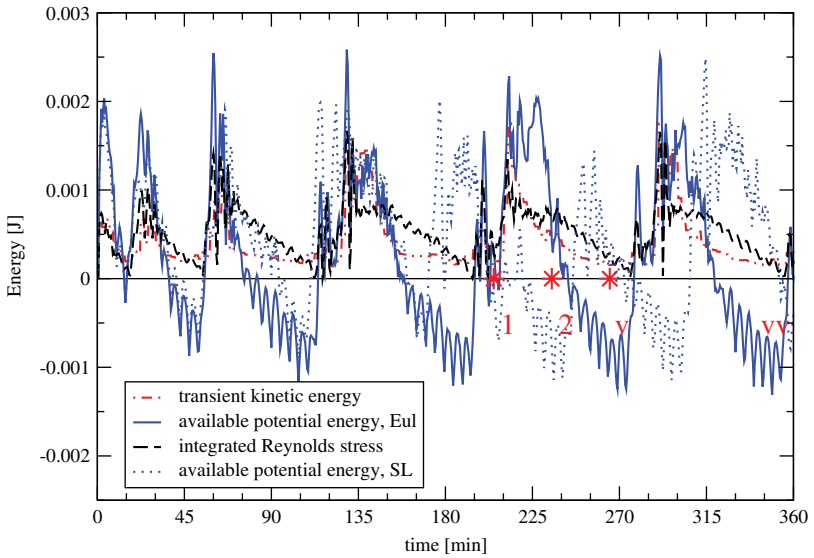

Figure 7. Time evolution of transient kinetic energy, available potential energy and the vertically integrated Reynolds stress for the flux-form Eulerian case (Eul). The corresponding flow situation for the individual markers (1–3) is shown in Figure 2. The dotted line denotes the available potential energy evolution for the corresponding semi-Lagrangian case (SL).

$\approx +1.4 \times 10^{-4}\%$ of the initial kinetic energy per time step. This adds to a 4–5 times larger non-conservative irreversible growth of (perturbation) background potential energy compared to the Eulerian case. This cannot be explained by enhanced mixing, since the cumulative contribution of diapycnal mixing is nearly the same for both schemes. It may be related to (artificial) irreversible external energy fluxes at the oscillating boundary. However, the non-conservative growth of the total energy (compared to the flux-form Eulerian case) does not appear to directly influence the flow evolution. But differences can be seen in the time evolution of the 'transient' energies, when comparing the available potential energy for the semi-Lagrangian and the Eulerian case in Figure 7. These match the altered corresponding flow evolution in plate (a) and (b) of Figure 1. It suggests that the advective-form numerical scheme contributes to the formation of critical layers in different spatial positions, which creates different bifurcation points for the flow development.

To clarify the role of numerical dissipation in comparison to the physical explicit viscous dissipation in the development of a mean flow reversal, it is instructive to assess the overall accumulated numerical dissipation. In the flux-form Eulerian case it is approximately four times the 'natural' cumulative viscous dissipation. This compares to a ratio of 11:1 in the viscous semi-Lagrangian case. This may imply an influence on the flow evolution. Figure 8 compares the equivalent inviscid simulations (without explicit viscosity, free-slip boundaries) of the laboratory setup for both, the flux-form Eulerian and the semi-Lagrangian case. In the inviscid case, the Eulerian simulation is also characterized by an irreversible growth of the kinetic energy, which—consistent with the viscous simulations—is about 2–3 times smaller than in the inviscid semi-Lagrangian case. Furthermore, an increased non-linearity is observed in

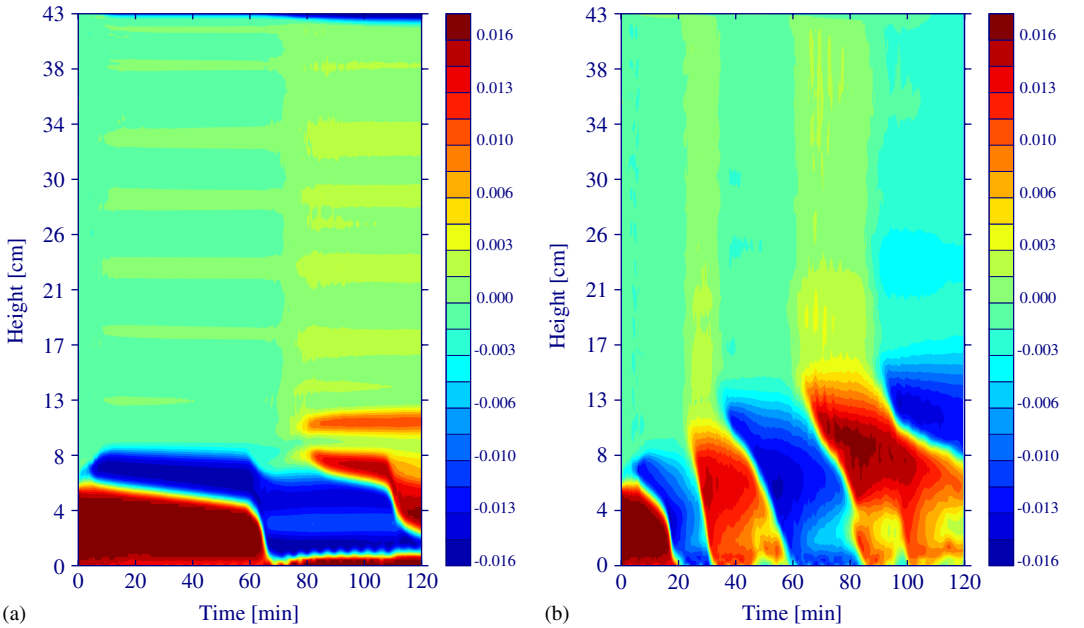

Figure 8. Time–height cross-section of the zonal mean flow velocity in the inviscid 2D numerical simulation using freeslip boundaries with a flux-form Eulerian advection scheme (plate (a)) and the same setup with a semi-Lagrangian advection (plate (b)).

the near membrane layers and in the shear region of the inviscid flow. The observation is also consistent with viscous simulations (starting from rest) with different membrane amplitudes, where we observed an earlier onset of a zonal mean flow oscillation with increased amplitudes. It is therefore speculated that an increased non-linearity of the simulated processes leads to a corresponding local increase in truncation error, which in return leads to the observed increase of kinetic energy growth. The results suggest that explicit viscous dissipation and numerical dissipation act similarly. Given the sensitivities with respect to decreasing explicit viscosity detailed in Reference [6] (i.e. longer period and lesser vertical extent of the zonal mean flow), the inviscid flux-form Eulerian simulation exhibits an asymptotically similar behaviour. With increased values of stratification ($\mathscr{S} = 0.36\,\mathrm{m}^{-1}$) the flux-form Eulerian simulation does not show a zonal mean flow oscillation and two strongly elongated vertically staggered mean flow layers develop (no oscillation would be expected from the theory of zonal mean flow interactions, in the absence of viscosity [26]). In comparison, the semi-Lagrangian simulation exhibits a physical solution, representative of increased viscosity. The results agree with the findings in Reference [27], where a flux-form Eulerian formulation, with a small viscosity explicitly added, gave closer agreement with the corresponding semi-Lagrangian simulation. Since in general flux-form schemes have higher-order truncation errors proportional to the differentials of fluxes of the primitive variables rather than to the differentials of the variables themselves (as characteristic of advective form schemes), the authors in Reference [27] concluded that the overall accuracy of the approximation increases when the fluxes of the

variables exhibit a greater degree of homogeneity than the variables themselves. This may be the case in the QBO analogue simulations with fairly steady wave momentum fluxes below the critical layer.

Errors in the domain-averaged, density-normalized inverse flow Jacobian $\mathscr{J} := (\rho_0^*/\rho^* J^{-1}) \equiv 1$, readily available in the semi-Lagrangian model simulation, are relatively small and maximal 2.5 percent. However, the errors occur in sensitive regions for this flow, in particular near the oscillating boundary and where wave overturning and breaking is observed. Notably, the time-step had to be reduced in the semi-Lagrangian simulation due to a too large 'Lipschitz' number $\mathscr{L} \equiv \| \Delta t \partial \bar{\mathbf{v}}^* / \partial \bar{\mathbf{x}} \|$ (cf. Reference [21] for a discussion). These findings also agree with the conclusions in Reference [28], where the flow was most in error above complex orography, as the semi-Lagrangian method looses local accuracy due to rapid changes in flow direction.

5. CONCLUSIONS

The energetic analysis described in Reference [9] has been useful in distinguishing between (numerically or physically caused) irreversible and reversible processes in our direct numerical simulations of the Plumb and McEwan laboratory experiment. Two simulations, using an advective-form semi-Lagrangian and a finite volume flux-form Eulerian advection scheme, respectively, have been compared by means of their energetic evolution. In the flux-form Eulerian case numerical dissipation acts to slightly decrease kinetic energy and to increase background potential energy from internal energy by an equal amount, conserving the total energy of the Boussinesq system to the order of round-off errors. This distinguishes the flux-form formulation from the semi-Lagrangian case, where unbalanced growth rates of background potential energy and kinetic energy lead to an overall increase of total energy. Our findings are consistent with the conclusions in Reference [29]. The authors compared semi-Lagrangian and flux-form Eulerian simulations of a double shear layer with a prescribed interface perturbation, where the advective-form algorithm develops an unphysical growth of kinetic energy, followed by an increased dissipation rate. The numerically caused growth of kinetic and background potential energy in our semi-Lagrangian simulation may arise in part out of a systematic, irreversible conversion from external energy directly or indirectly enforced through the (oscillating) boundary. Nevertheless, the physical significance is unclear, since the accumulated growth contributes to the growth of background potential energy, which does not have a direct influence on the flow evolution.

An important aspect of the flow analysis is given by the time evolution of the irreversible instantaneous exchange rates and subsequently the time evolution of available potential energy. Three inherently different volume-averaged measures, available potential energy, transient kinetic energy and the absolute of the vertically integrated Reynolds stress similarly characterize the flow evolution. In particular, these differ for the flux-form Eulerian and the semi-Lagrangian case, matching their altered flow evolution. It identifies the semi-Lagrangian solution as a more viscous, physically incorrect account of the instantaneous reversible and irreversible fluxes, primarily due to enhanced numerical dissipation which in return contributes to the development of different bifurcation points of the flow evolution. The described numerical sensitivities are relevant in our simulations, where the large-scale flow is driven by small-scale fluctuations, but may apply to simulations of the atmospheric QBO and geophysical

flows in general. In particular, this may be important for the future design of high resolution weather and climate models, since state-of-the-art numerical weather prediction relies on the efficiency of semi-Lagrangian methods. Thus, the energy diagram in Figure 3 has been complemented by the potential contributions of the numerics of the simulation, in particular, where the interplay of reversible and irreversible fluxes determines the flow evolution.

ACKNOWLEDGEMENTS

I wish to thank Dr Piotr Smolarkiewicz for his extensive comments on the original manuscript. Comments from the two anonymous reviewers were appreciated. The research formed part of a PhD thesis at the Ludwig-Maximilians-Universität München under the supervision of Prof. Dr Ulrich Schumann (Deutsches Zentrum für Luft- und Raumfahrt).

REFERENCES

1. Schumann U. Direct and large eddy simulations of stratified homogeneous shear flows. *Dynamics of Atmospheres and Oceans* 1996; **23**:81–98.
2. Staquet C, Sommeria J. Internal gravity waves: from instabilities to turbulence. *Annual Review of Fluid Mechanics* 2002; **34**:559–593.
3. Baldwin MP, Gray LJ, Dunkerton TJ, Hamilton K, Haynes PH, Randel WJ, Holton JR, Alexander MJ, Hirota I, Horinouchi T, Jones DBA, Kinnersley JS, Marquardt C, Sato K, Takahashi M. The quasi-biennial oscillation. *Reviews of Geophysics* 2001; **39**(2):179–229.
4. Plumb RA, McEwan D. The instability of a forced standing wave in a viscous stratified fluid: a laboratory analogue of the quasi-biennial oscillation. *Journal of the Atmospheric Sciences* 1978; **35**:1827–1839.
5. Wedi NP, Smolarkiewicz PK. Laboratory for internal gravity-wave dynamics: the numerical equivalent to the quasi-biennial oscillation (QBO) analogue. *International Journal for Numerical Methods in Fluids* 2005; **47**:1369–1374.
6. Wedi NP. Time-dependent boundaries in numerical models. *Ph.D. Thesis*, Ludwig-Maximilians-Universität München, LMU München, 2004. http://edoc.ub.uni-muenchen.de/archive/00003142
7. Kondepudi D, Prigogine I. *Modern Thermodynamics—From Heat Engines to Dissipative Structures*. Wiley: New York, 1998.
8. Galmiche M, Thual O, Bonneton P. Wave/wave interaction producing horizontal mean flows in stably stratified fluids. *Dynamics of Atmospheres and Oceans* 2000; **31**:193–207.
9. Winters KB, Lombard PN, Riley JJ, D'Asaro EA. Available potential energy and mixing in density-stratified fluids. *Journal of Fluid Mechanics* 1995; **289**:115–128.
10. Holloway G. The buoyancy flux from internal gravity wave breaking. *Dynamics of Atmospheres and Oceans* 1988; **12**:107–125.
11. Dörnbrack A. Turbulent mixing by breaking gravity waves. *Journal of Fluid Mechanics* 1998; **375**:113–141.
12. Laprise R, Peltier WR. The linear stability of nonlinear mountain waves: implications for the understanding of severe downslope windstorms. *Journal of Atmospheric Sciences* 1989; **46**:545–564.
13. Laprise R, Peltier WR. The structure and energetics of transient eddies in a numerical simulation of breaking mountain waves. *Journal of Atmospheric Sciences* 1989; **46**:565–585.
14. Lorenz ED. Available potential energy and the maintenance of the general circulation. *Tellus* 1955; **VII**(2): 157–167.
15. Ozawa H, Ohmura A, Lorenz RD, Pujol T. The second law of thermodynamics and the global climate system: a review of the maximum entropy production principle. *Reviews of Geophysics* 2003; **41**(4):1–24.
16. Prusa JM, Smolarkiewicz PK. An all-scale anelastic model for geophysical flows: dynamic grid deformation. *Journal of Computational Physics* 2003; **190**:601–622.
17. Smolarkiewicz PK, Prusa JM. Towards mesh adaptivity for geophysical turbulence. *International Journal for Numerical Methods in Fluids* 2005; **47**:789–801.
18. Wedi NP, Smolarkiewicz PK. Extending Gal-Chen & Somerville terrain-following coordinate transformation on time-dependent curvilinear boundaries. *Journal of Computational Physics* 2004; **193**:1–20.
19. Smolarkiewicz PK, Prusa JM. Forward-in-time differencing for fluids: simulation of geophysical turbulence. In *Turbulent Flow Computation*, Drikakis D, Guertz BJ (eds). Kluwer Academic Publishers: Dordrecht, 2002; 207–240.
20. Smolarkiewicz PK, Margolin LG. On forward-in-time differencing for fluids: extension to a curvilinear framework. *Monthly Weather Review* 1993; **121**:1847–1859.

21. Smolarkiewicz PK, Pudykiewicz JA. A class of semi-Lagrangian approximations for fluids. *Journal of Atmospheric Sciences* 1992; **49**:2082–2096.
22. Smolarkiewicz PK, Margolin LG. MPDATA: a finite difference solver for geophysical flows. *Journal of Computational Physics* 1998; **140**:459–480.
23. Smolarkiewicz PK, Grell GA. A class of monotone interpolation schemes. *Journal of Computational Physics* 1992; **101**:431–440.
24. Smolarkiewicz PK, Margolin LG. Variational methods for elliptic problems in fluid models. *Proceedings of the ECMWF Workshop on Developments in Numerical Methods for Very High Resolution Global Models*, Reading, U.K., Eur. Cent. For Medium-Range Weather Forecasts, 2000; 137–159.
25. Gill A. *Atmosphere-Ocean Dynamics*, *Vol. 30*, *International Geophysics Series*. Academic Press: London, 1982.
26. Plumb RA. The interaction of two internal waves with the mean flow: implications for the theory of the quasi-biennial oscillation. *Journal of Atmospheric Sciences* 1977; **34**:1847–1858.
27. Smolarkiewicz PK, Margolin LG. On forward-in-time differencing for fluids: an Eulerian/semi-Lagrangian non-hydrostatic model for stratified flows. *Atmosphere-Ocean Special* 1997; **35**:127–152.
28. Cullen M, Salmond D, Smolarkiewicz PK. Key numerical issues for the future development of the ECMWF model. *Proceedings of the 2000 Workshop on Developments in Numerical Methods for Very High Resolution Global Models*, Reading, U.K., Eur. Cent. For Medium-Range Weather Forecasts, 2000; 183–206.
29. Drikakis D, Margolin LG, Smolarkiewicz PK. On 'spurious' eddies. *International Journal for Numerical Methods in Fluids* 2002; **40**:313–322.

